RPC-LAP Cross-Calibration Report

Anders I. Eriksson, Fredrik Leffe Johansson, Erik P. G. Johansson, Elias Odelstad

RO-IRFU-LAP-XCAL

Version 1.0

December 17, 2019

Contents

1 Introduction

1.1 Scope and structure

This document describes the cross-calibration methods performed to obtain several parameters available in the Rosetta Dual Langmuir Probe (LAP) DERIVED archive delivered to the ESA Planetary Science Archive (PSA, made available at https://www.cosmos.esa.int/web/psa/rosetta), and also describes the validation of the data products. The cross-calibration is performed by comparison to the measurements of two other instruments in the Rosetta Plasma Consortium (RPC), the Mutual Impedance Probe (MIP), and the Ion Composition Analyser (ICA) as well as an internal cross-calbration between different modes and analysis methods of LAP itself. In addition, data from the ROSINA-COPS sensor is used for one validation (Section 7).

The spacecraft potential estimate is fundamental to the interpretation of plasma data. When negative, comparison data can be obtained by ICA, as reported in Section 2. The various methods of obtaining the spacecraft potential from LAP data are compared in Section 3. The most interesting parameter for many users probably is the plasma (electron or ion) number density. Values derived from LAP probe bias sweeps are compared to MIP measurements in Section 4, and a general cross-calibration of high time resolution LAP data to MIP in Section 5. The probe photoelectron emission saturation current may not be a fundamental plasma parameter in itself, but as it is a proxy for the solar EUV flux it is nevertheless of interest and the various methods for deriving it from LAP data are compared in Section 6. It is also needed for estimation of ion flow speed, which is the topic of Section 7. Finally we discuss the LAP electron temperature estimates in Section 8.

1.2 Relation to other documents

The focus of this document is the physics of the cross-calibration and motivation and validation of the analysis performed in the LAP DERIVED archive. It can be seen as a reference document for the LAP User Guide (UG), which is intended as a practical introduction for a new user of LAP science data. For more details on data formats and algorithms please see the LAP Experiment to Archive Interface Control Document (EAICD). Both these documents are available in the PSA.

A cross-calibrated electron density product based on LAP and MIP data is also available in the RPC-MIP archive. The corresponding documents for MIP (user guide, EAICD and cross-calibration report) may therefore also be of interest to a user. These are available in the MIP archive on the PSA.

The LAP UG and EAICD are referred to by these abbreviations in the rest of this report. Apart from archive documents, several studies relevant for calibration and validation have been published as scientific papers. These are referenced by author and date, with a reference list at the end.

2 LAP-ICA spacecraft potential cross-calibration

2.1 Spacecraft potential measurements by LAP and ICA

The spacecraft potential V_s is set by the balance of currents due to impacting plasma electrons and emitted electrons (photoemission as well as secondary emission due to particle impact) as illustrated in Figure 1 [Odelstad et al., 2015, 2017]. As this balance depends on the plasma parameters, particularly the electron density, it can be used for monitoring plasma parameters. This is used for deriving the N_EL and N_ED plasma density estimates available in the LAP data and the calibration of V_s to plasma density is discussed elsewhere in this report (Section 5). In the present Section we concentrate on how the LAP V_s estimates compare to ICA observations of ions.

As described in the LAP UG, the s/c potential V_s is found from LAP data by identifying either the floating potential of the probe V_z (the voltage, with respect to spacecraft ground, at which all currents between probe and the surrounding plasma add to zero) or the photoelectron emission "knee" potential V_{ph} (Figures 2 and 3) in the observed LAP probe characteristic (current-voltage curve). In the LAP archive, the resulting V_s estimates are known as U_SC and V_PH_KNEE, respectively. The consistency of the two estimates are discussed in Sections 3 & 5.2. As V_s derived in this way turns out to be negative during most of the Rosetta mission (Figure 4), V_s should also be accessible by ICA as the lower cutoff energy of the observed ions: as all ions are accelerated toward the spacecraft, none should reach it with lower energy than $e\,V_s$ (Figure 5).

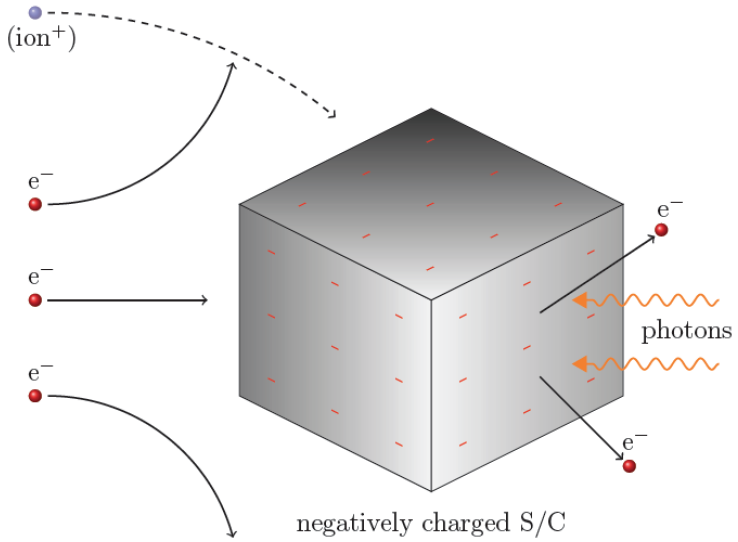

Figure 1: The spacecraft potential is set by the balance of currents due to impacting plasma electrons and emitted electrons (photoemission as well as secondary emission due to particle impact). Illustration by Odelstad [2018] for typical Rosetta case of a negatively charged spacecraft.

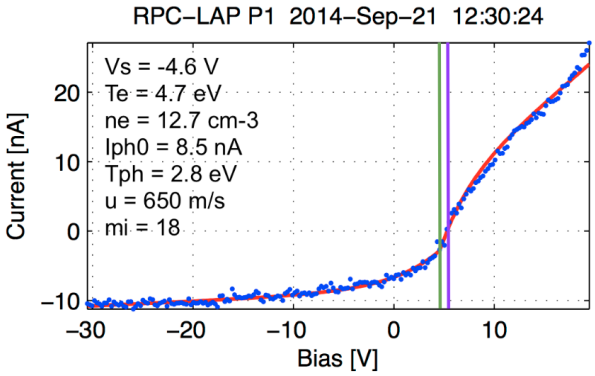

Figure 2: An example LAP probe bias voltage sweep with data points in blue and a fit to the standard theoretical model of Figure 3 in red. The V_s value obtained from the fit actually is V_{ph}, marked by a green vertical bar. We obtain V_z as the negative of the bias voltage where the current is zero (magenta line).

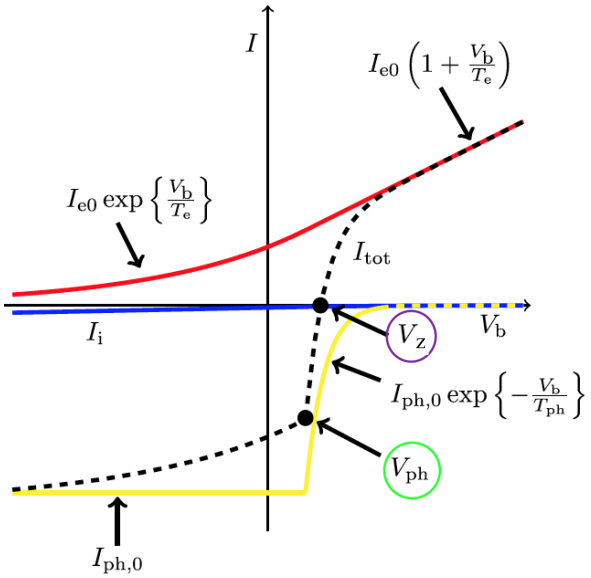

Figure 3: Sketch showing the contributions to the total probe current I (dashed) from photoelectron emission (yellow), plasma ions (blue) and plasma electrons (red). Here I_{e0} and I_{i0} are proportional to the density and characteristic speeds of electrons and ions, respectively, while I_{ph0} depends on the solar EUV intensity and material properties of the probe. The two V_s estimates V_z and V_{ph}, corresponding to the archived quantities U_SC and V_PH_KNEE, are highlighted by magenta and green circles, respectively. More information on the theoretical model is available in Eriksson et al. [2017].

2.2 Comparison of LAP and ICA V_s estimates

As the techniques are independent, comparing LAP and ICA measures of V_s is an excellent cross-calibration. For ICA, the chief error source is an internal offset of the instrument voltages, while the principal uncertainty for LAP is how large a fraction of V_s remains at the probe position (Figure 7). By comparing the data from the two instruments, it should be possible to determine the factor for LAP and the offset for ICA. The example in Figure 6 shows a time interval where ICA was run in high time resolution (HR) mode, providing an energy spectrum every 4 s. Only data of this type have been used for comparison to LAP, as the very large plasma variations encountered on time scales longer than ~10 s means the cutoff due to V_s can be hard to define in ICA data. It is also necessary to put data selection restrictions on ICA sensor temperature, as this affects ICA energy offsets. We found 8.5°C to be a practical limit [Odelstad et al., 2017]. With these constraints, useful ICA HR data can be found intermittently from end of May 2015 to late August 2016. To obtain consistent data for comparison, available ICA HR data from this period were further separated into smaller blocks as other operational settings changed, typically a few hours in duration.

Figure 8 shows two examples of how the LAP and ICA V_s estimates from these intervals relate to each other. In both cases a linear relation can be discerned, with some scatter. The slope of the fitted line is close to 1 in both cases, suggesting that LAP picks up almost all of V_s. However, the derived value of this factor is not always 1, as can be seen in the left panel of Figure 9 displaying the fit coefficients for all intervals meeting the selection criteria. The ICA offset at right is not of primary interest interest for this report but is shown at right for completeness; we may note that it now is used in the ICA calibration process.

The factor obtained from the fit, shown at right and interpreted as the fraction of V_s picked up by LAP, is seen to vary between intervals. Some random scatter is expected, as there is nothing forcing the plasma to always contain ions with energy down to zero in the s/c frame of reference, which is the assumption behind the ICA method, and considering inevitable noise in the data from both instruments. Such noise, and additional sources from the data analysis and also in the measurements themselves, should be the reason for the values above 1 which are otherwise unphysical. If viewing these points with suspicion, one may then wonder about the points at the other extreme, around 0.7, but it can be noted that several of these have small error bars suggesting good quality. No consistent way of relating the fraction to other quantities in LAP data has been found [Odelstad et al., 2017]. We conclude that while the data admits the fraction of V_s picked up by LAP to vary between 0.7 and 1.0, with an average possibly around 0.9, we cannot reliably determine a value for this fraction. In consequence, there has been no attempt to correct for this fraction in the LAP V_s estimates in the LAP archive data, but we can conclude that the absolute accuracy of any LAP V_s estimate is on the order of about 20%.

The most important conclusion from Figure 9 is that despite some scatter, the LAP and ICA V_s estimates relate to each other basically as expected. This consistency validates the use of any of these estimates for V_s.

The panel at right in Figure 8 also suggests an offset between the LAP V_s estimates by V_z and V_{ph}. This will be further discussed in Section 3.

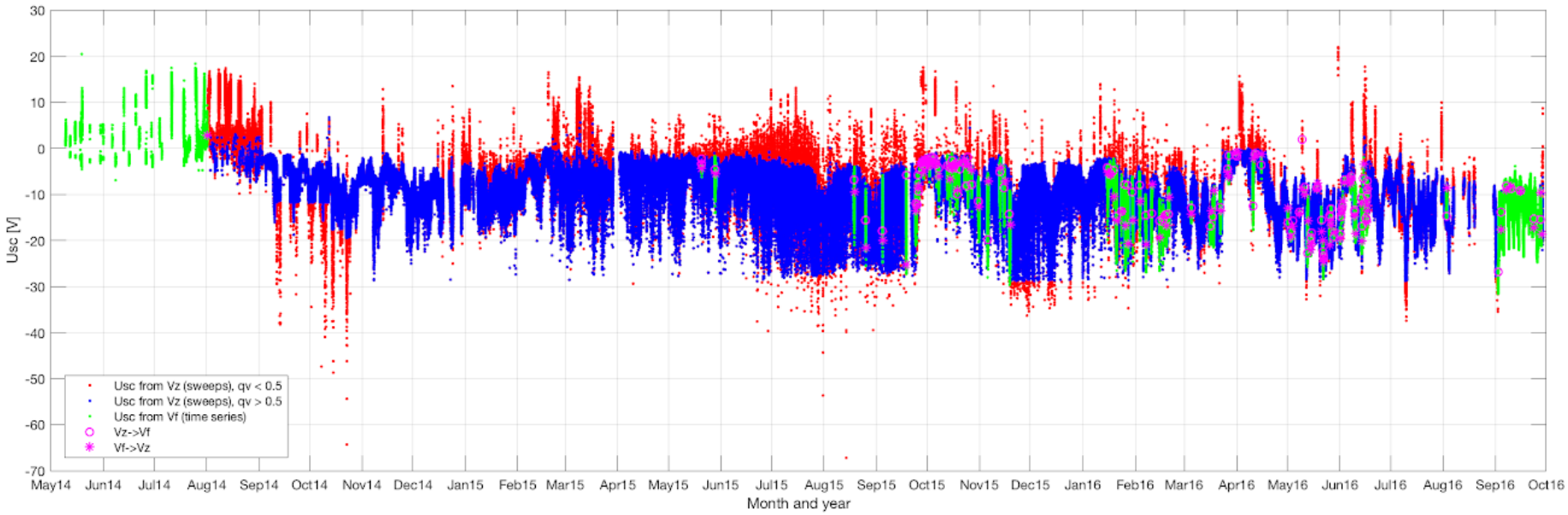

Figure 4: LAP V_s overview for the main Rosetta mission (May 2014 through September 2016). Red and blue dots are obtained from the floating potential found in LAP probe bias sweeps. As described in the LAP EAICD, data points are assigned a quality value between 0 and 1: here blue dots are high quality data ($q \geq 0.5$) while red points are low quality ($q < 0.5$). Green dots mark estimates based on voltage measurements of probes at a bias current (prior to May 2015) or floating (from May 2015).

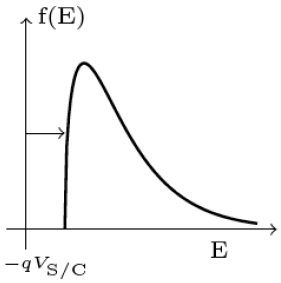

Figure 5: The spacecraft potential accelerates ions toward the spacecraft, shifting (and distorting) the energy distribution of ions entering ICA. From Odelstad [2018].

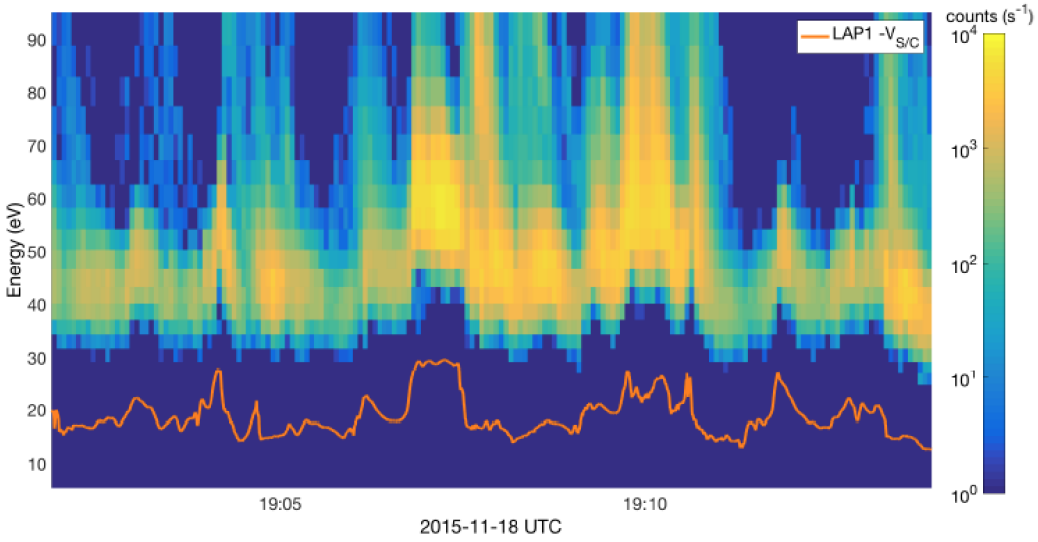

Figure 6: An example of comparison of ICA ion energy spectra to LAP V_s estimates [Odelstad, 2018].

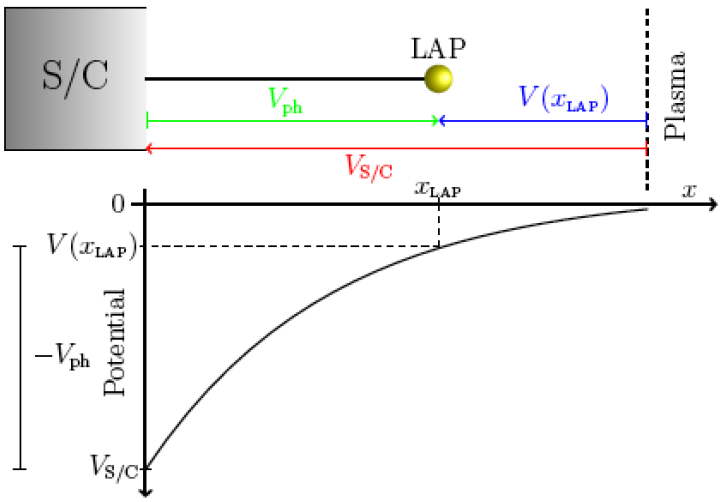

Figure 7: The negative charge on the spacecraft forms an electrostatic field around it, which has not decayed to zero at the location of the probe. In consequence, the measured probe-to-spacecraft potential only represents some fraction of V_s. After Odelstad [2018].

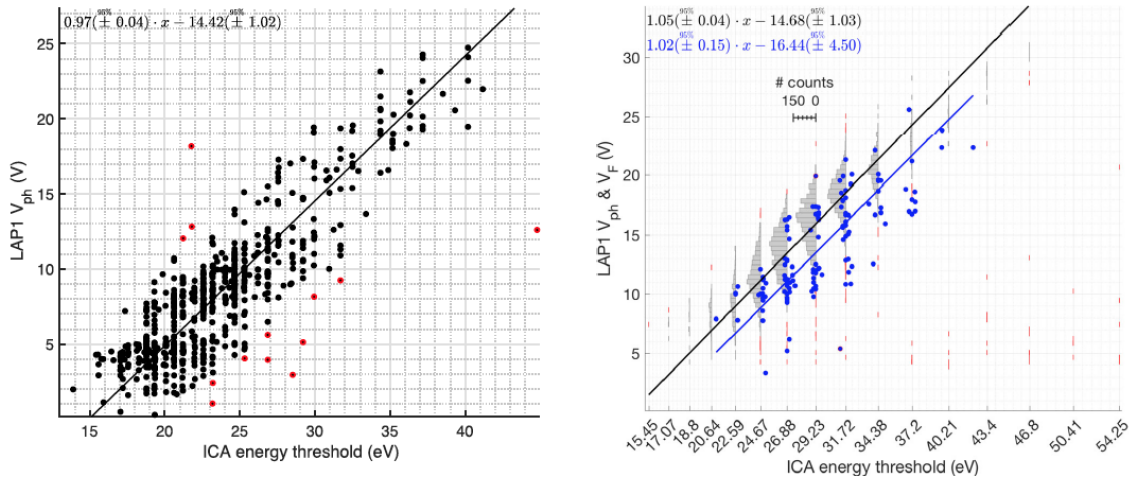

Figure 8: Two examples of the relation between LAP and ICA V_s estimates, with linear least squares fits indicated. *Left:* Data from 2015-07-16 07:32 – 11:00 UT. The LAP V_s estimate here is based on identifying the photoelectron knee in LAP sweeps. *Right:* Data from 2016-01-20 22:00 UT – 2016-01-21 15:00 UT. LAP obtained floating potential observations (V_z values, shown as grey histograms) in the first half of this interval and was sweeping in the second half (V_{ph} values, shown as blue dots). From Odelstad et al. [2017].

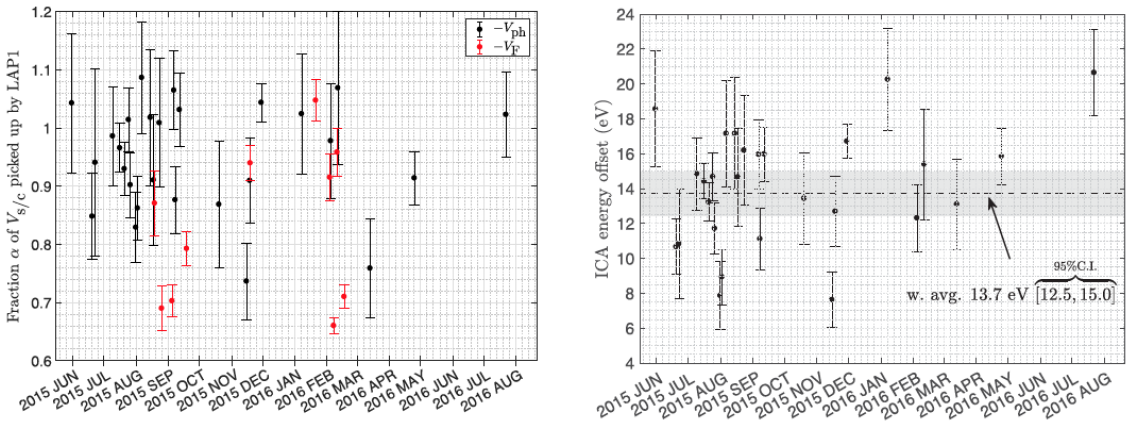

Figure 9: Overview of the factor and offset in the linear relation of LAP to ICA V_s estimates from fits as in Figure 8, with error bars indicating 95% confidence intervals. *Left:* The factor, interpreted as the fraction of V_s picked up by LAP. *Right:* The offset, intepreted as an ICA energy offset, together with the mean of all values (dashed line, weighted by the inverse variance of the fit within each interval) and the 95% confidence interval (shaded) for this mean. Figure from Odelstad et al. [2017].

3 LAP spacecraft potential estimates

LAP (as well as ICA and IES) regulates the attraction or repulsion of the measured particles by applying voltages to the detectors. The ground potential for the applied bias voltage is the spacecraft potential V_s with respect to infinity[1]. The value of V_s is determined by the requirement that the total net current to the spacecraft is zero [Odelstad et al., 2017]. Most of the spacecraft surfaces (including solar cell cover glasses) are conductive and connected to this ground, to make V_s well defined and regulated by the plasma properties.

The s/c potential can be found from LAP data in several ways:

- V_{ph} – negative of the bias voltage (V_b) of the photoelectron knee observed in LAP bias sweeps. At higher bias voltages, the photoemission decreases approximately exponentially, while it is constant at lower bias values, giving a distinct knee Eriksson et al. [2017].
- V_z – negative of the bias voltage in a LAP sweep for which the resulting probe current is zero.
- V_f – negative of the measured voltage of a LAP probe when the probe is left "floating", i.e. with the bias circuitry disconnected so that no current flows to or from the probe.

Figure 2 shows an example LAP bias voltage sweep with V_{ph} and V_z indicated.

In an ideal case, V_z and V_f should be fully equivalent. However, as the sweep has a discrete step size, 0.25 or 0.5 V in most LAP modes but sometimes more, and that V_z has to be found by some sort of interpolation or fitting, V_z usually shows more noise than does V_f, which also is immune to any possible displacement current added when varying the bias voltage. Perhaps even more importantly, the identification of V_z rely on an exact identification of leakage currents in the offset calibration, which V_f do not. However, the method of fitting V_z can theoretically increase the range of the estimate beyond the sweep window. In Figure 10 we show a validation of the automatic identification of V_z, beyond the sweep range, and in comparison to V_f and ICA spacecraft potential estimates. No obvious discontinuities are seen between two methods in Figure 10, but on a statistical estimate over the mission, as shown in Figure 11, we find a slight shift with a median of 0.4 V.

A sweep with noise or disturbances can have several zero-crossings of current. In these cases, the zero-crossings are ranked in order of longevity, i.e. the distance to the next zero-crossing in either direction, as we find that these disturbances are usually short-lasting. Only the best ranked zero-crossing is evaluated for a V_z estimate, and the quality value is set to a lower value.

The photo-electron knee V_{ph} is found at a peak in the second derivative of the current and needs as such a very good signal-to-noise ratio to recover an accurate estimate. Unfortunately, the dynamic environment and highly negative spacecraft potential during the mission conspired to make this estimate very hard to obtain. Some very negative and highly positive artefacts are visible in Figure 12. Nevertheless, V_{ph} should provide a better estimate of the spacecraft potential when the potential is low or positive as the floating potential offset from V_s increases non-linearly. This has not been taken into account for the LAP main s/c potential estimate, U_SC in the USC files, but for the cross-calibration of the s/c potential to plasma density we have included a splicing to V_{ph} for low and positive potentials as described in Section 5.2.

[1] This definition is not fully stringent in the presence of electric fields in the plasma. An alternative definition of V_s is as the potential of the spacecraft with respect to what the potential in space at the position of the spacecraft would have been if the spacecraft was not there.

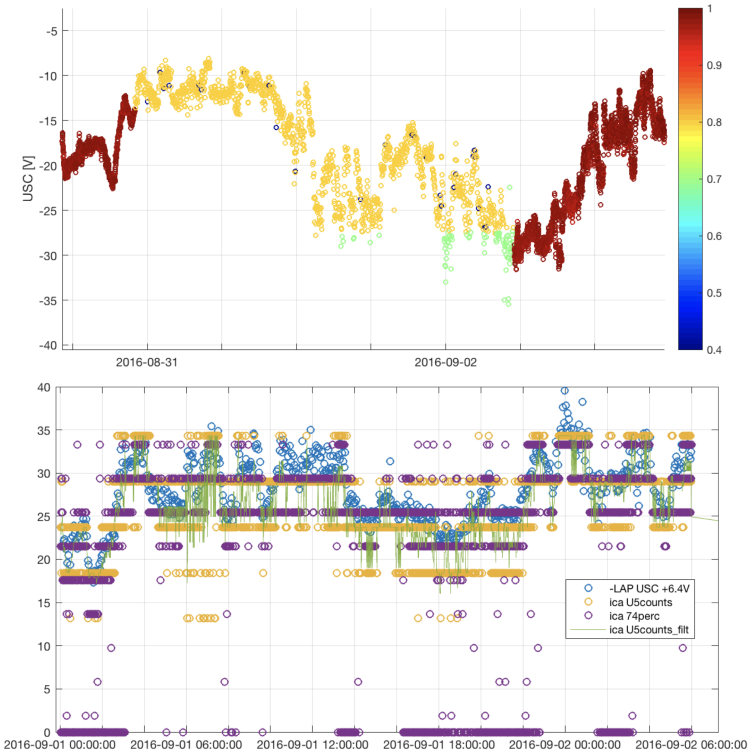

Figure 10: **Top:** comparison of V_z and V_f, coloured by quality value. Green circles are extrapolated V_z values beyond sweep range, yellow circles are good quality V_z, and V_f is indicated by different shades of red circles. **Bottom:** Comparison of U_SC data (blue circles) with an added ICA offset as discussed in Section 2 and ICA estimates of spacecraft potential from lowest energy bin of ions; several methods in yellow and orange, and low-pass filtered in green. Note that the time period of the two plots partly overlap, extrapolated value (above 34 in the bottom plot) agree with ICA estimates and there are no obvious discontinuities in moving from V_z to V_f in the top plot

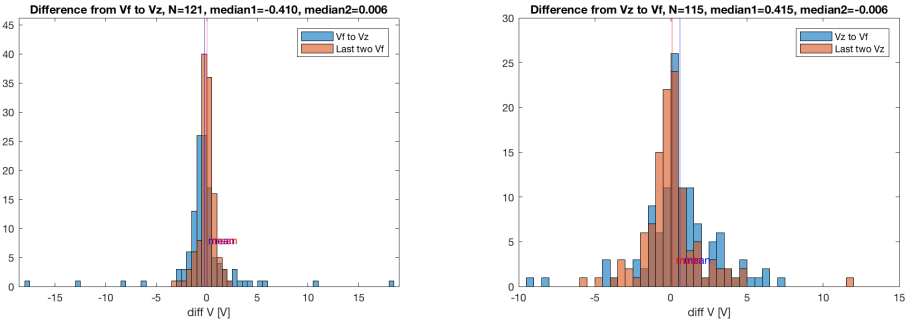

Figure 11: Histograms of the transition between two USC methods, in comparison to difference between the two previous measurement. **Left:** from V_f to V_z. **Right:** from V_z to V_f. The mean difference is marked with vertical lines

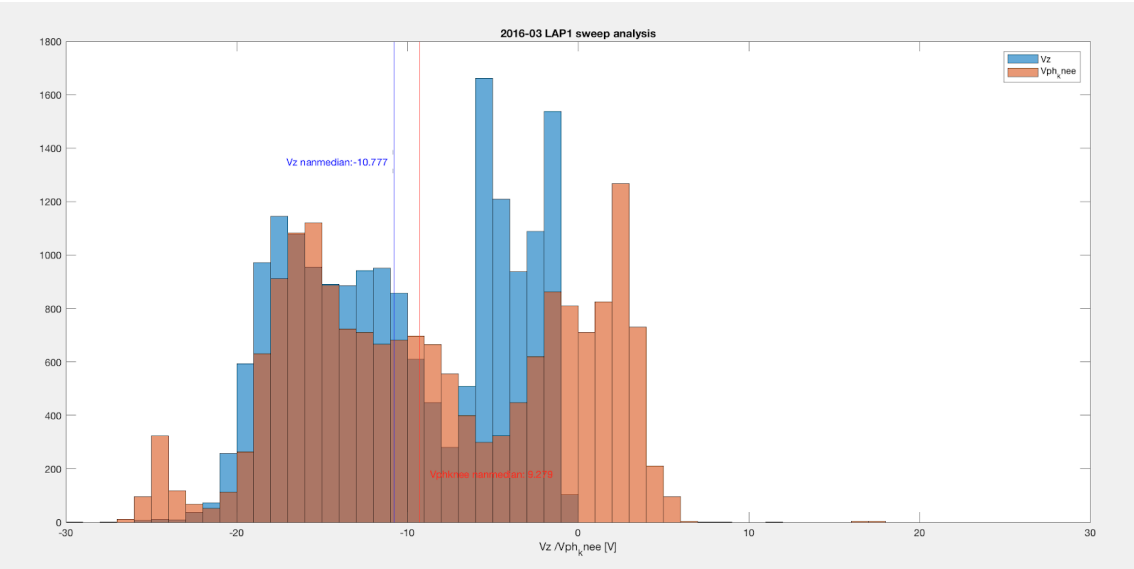

Figure 12: Histogram of V_{ph} (red) and V_{z} (blue) estimates over a month of data. The peaks of the V_{ph} histogram around -24 V and >8 V are artefacts related to voltage range of some operational modes. Note that V_{z} falls off sharply just before 0 V, consistent with V_{ph} being a better estimate of the spacecraft potential around and above zero.

4 Electron density from LAP sweep slope and comparison to MIP

This method to find the plasma density is based on the slope of LAP probe bias sweeps on the electron collection side of the current-voltage characteristic, corresponding to positive bias voltage and seen as the linear part at far right in Figures 2 and 3. This slope is re-scaled to plasma density using an assumed T_e value. While an advantage with this is that any random errors in the determination of T_e will not enter the density data, an obvious problem is that T_e may not be constant. This can be seen directly in the all-mission histograms of the electron slope (upper left in Figure 13), which show two distinct peaks, separated by a minimum at 70 nA/V (highlighted by the magenta line). Engelhardt et al. [2018] identified the peak at high slopes as due to cold electrons, with an effective temperature around or below 0.1 eV. Consistent with their results, Figure 13 shows this high-slope peak as a constant feature of all months from November 2014 through March 2016, with some minor hints also in April and May of the latter year. We can see that the limit value 70 nA/V is quite constant through all months. Around perihelion (July through September 2015) sweeps with this high slope are common. The months of March and April 2016 also show another minimum in the histograms, at around 4 nA/V (green line).

The top plot in Figure 14 shows the electron slope in all LAP1 sweeps acquired during the comet mission. In total, 388,901 sweeps (blue) are included, of which 83,039 (about 20%, green) have simultaneous MIP density measurements (within 2 s). As the slope is proportional to plasma density, it is no surprise to see that the highest slopes cluster around perihelion (August 2015), or the low slopes mainly in the early mission phase and during the night-side excursion in late March - early April 2016.

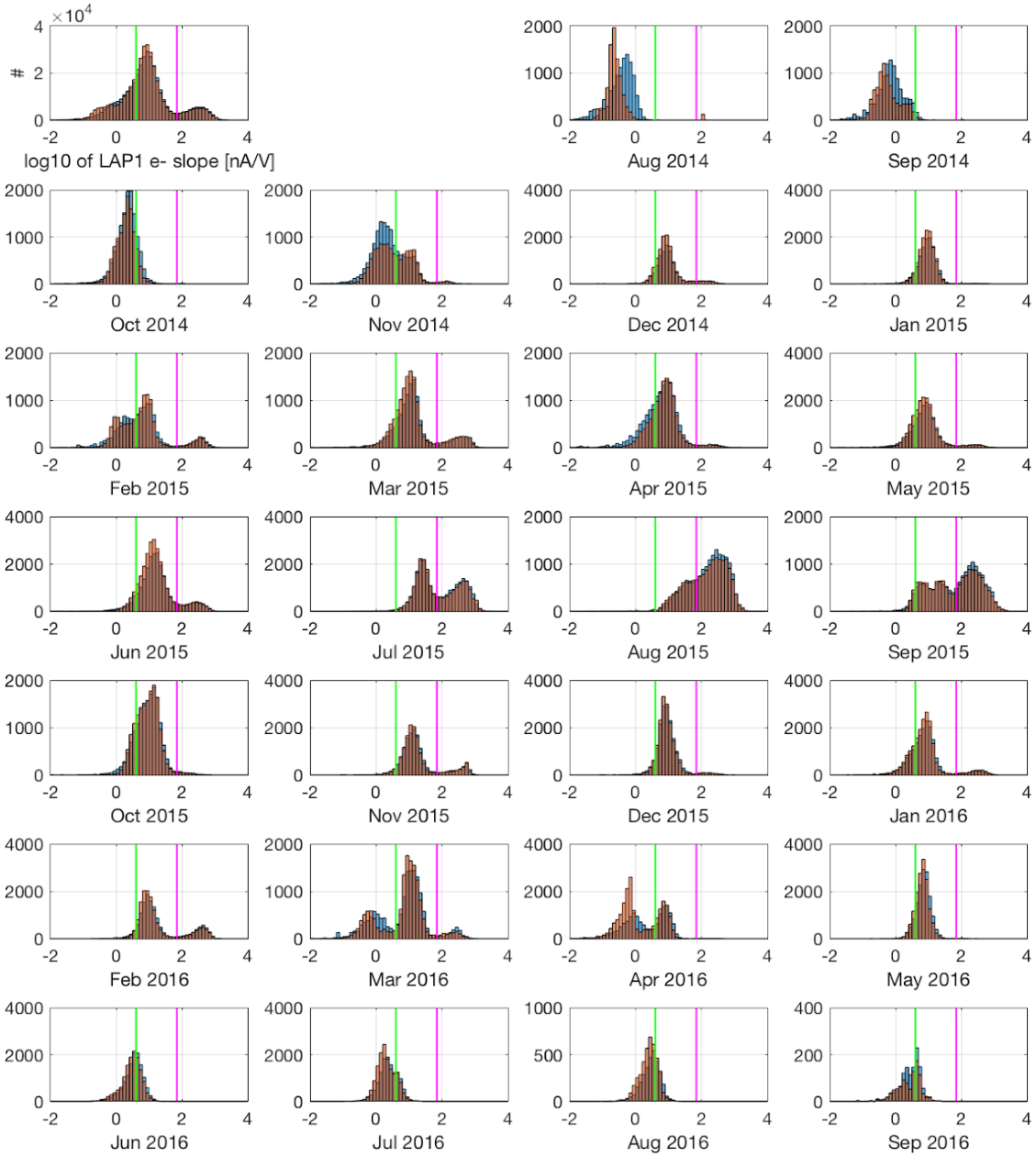

Figure 13: Histograms of LAP electron current slopes. At top left is a mission-wide histogram, the rest are sorted per month. The green and magenta vertical lines are placed at 4 and 70 nA/V, respectively. It can be seen that 70 nA/V is a stable minimum, suitable for use as divisor between sweeps dominated by warm and cold electrons.

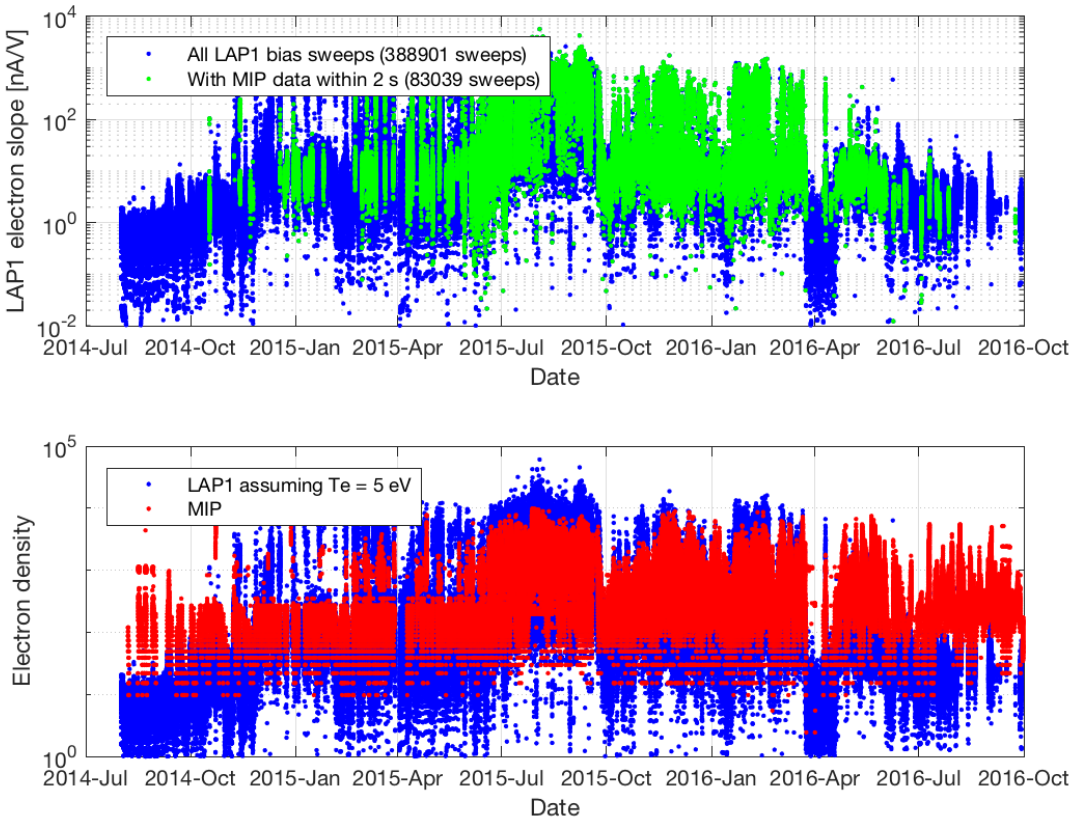

Figure 14: **Top.** LAP1 electron slopes. Green indicates when simultaneous MIP densities are available. **Bottom.** LAP1 (blue, assuming $T_e = 5$ eV) and MIP (red) electron densities.

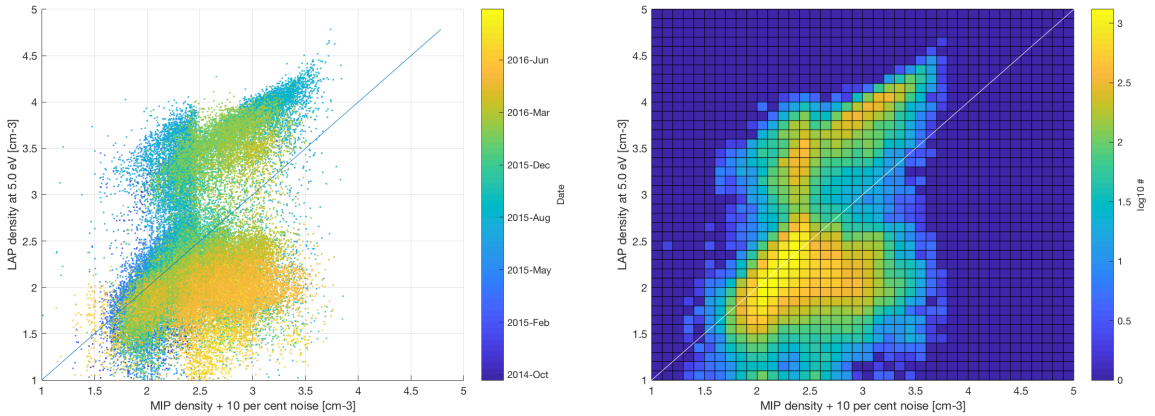

Figure 15: Electron density measurements within two seconds of each other, over all the comet mission. In the plot, ten per cent noise has been added to the MIP data to avoid coarse discretization.

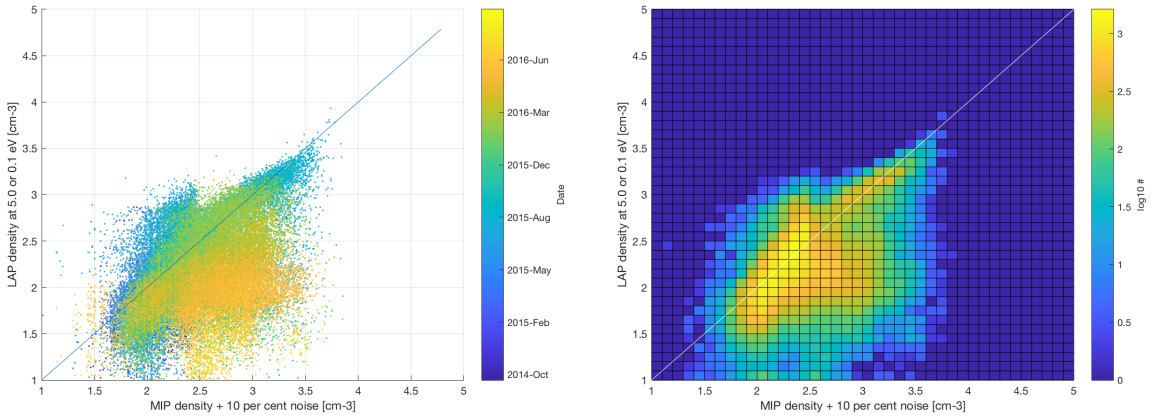

Figure 16: The same data as in Figure 15, with assumed T_e set to a lower value T_c (indicated in the vertical labels) for points with electron slope higher than 70 nA/V.

The bottom plot in the same Figure 14 shows the MIP plasma density from the same period in red. During parts of the mission, a cutoff around 300 cm^{-3} can be seen, expected because of the high-density limitation of the MIP LDL mode. The density calculated from the LAP electron slope, scaled to plasma density assuming $T_e = 5$ eV is shown in blue. While the errors in LAP can be large at low density, it is notable that values below 10 cm^{-3} are mostly seen in the months where solar wind densities could be expected: the arrival in August and September 2015, early April 2015 when Rosetta had to leave the immediate vicinity of the nucleus because of navigation problems induced by high dust activity, and during the night-side excursion in late March and early April 2016. These low densities are below the MIP measurement range, and the discrepancy between LAP and MIP here is expected. Another obvious difference in the plot is the higher densities often seen by LAP around perihelion. The high density range is where MIP is most reliable, so the explanation should be within LAP and is readily found to be the presence of a cold plasma with T_e much below the 5 eV assumed in the calibration, i.e. the electron population causing the peak below 70 nA/V in the histograms in Figure 13 [Engelhardt et al., 2018].

The simultaneous LAP and MIP densities in the bottom panel of Figure 14 are displayed versus each other in Figure 15, with the colour code indicating date. As $T_e = 5$ eV has been used for the LAP data, the sweeps with steep slopes from the presence of colder electrons will indicate too high electron density, which we see as the detached cloud of points in the upper half of the plot. As we above found a consistent limit of 70 nA/V for these, we can adjust the value of T_e used for these sweeps. This is done in Figure 16, where we find that a value $T_e = 0.15$ eV for all sweeps with slope higher than 70 nA/V make the points cluster around the line of slope one.

The large yellow-orange blob below the slope-1 line in Figure 16 indicates a remaining problem with

the late part of the mission, from May 2016 onwards. For this phase, the LAP density mostly turns out much lower than the MIP value when the latter is above about 200 cm^{-3}. MIP data are expected to be good in this range.

5 LAP-MIP cross-calibrated densities

The mutual impedance and Langmuir probe techniques implemented by the MIP and LAP instruments, respectively, well complement each other for the study of cold and thermal plasma. The chief advantage of MIP is that it estimates the density from the plasma frequency, which depends on no other parameter, while LAP works with fluxes of ions and electrons depending also on particle energies. For the plasma density, LAP on the other hand benefits from high sampling rate and high dynamic range. MIP has a limited sensitivity range, and often a much lower sampling rate. Both instruments should be influenced by the perturbations the charged spacecraft imposes on its environment, though in practice MIP sounds a much larger and less disturbed volume than that from which a LAP probe collects its current, so MIP usually is affected less by such problems than the LAP probe currents. The LAP spacecraft potential estimates are on the other hand quite robust, but needs calibration to some absolute density value to be converted to plasma density. We attempt therefore to obtain a better density data set by combining LAP superior sampling rate, resolution and cometary mission coverage by cross-calibrating the LAP measurements in various modes with MIP. We here describe two such data products (N_ED and N_EL) in the LAP archive; a third is available in the MIP data archive.

An in-situ measurement on Langmuir probes on short booms well inside the electrostatic potential field of a highly negative spacecraft results in a much reduced electron flux than in the undisturbed plasma as the spacecraft often effectively shields the probe from the lowest energy electrons. This effect is clear when comparing ion currents and electron currents obtained at fixed bias voltage, so that the actual probe bias voltage to the plasma varies with the spacecraft potential. An overview of such data from the entire mission is shown in Figure 17. The LAP archive therefore does not include any plasma density product based on probe current measured by a probe at fixed positive bias voltage. The effect does not exist for ion current (current to a negatively biased probe, for a sunlit probe also including the photoemission current) or for the LAP s/c potential estimates, so such LAP data are suitable for cross-calibration with MIP plasma density. Note that the positive bias voltage range is included for the N_E_FIX_T_E electron density estimate (Section 4) derived from the slope as seen in probe bias voltage sweeps, which is less affected (though not immune) to this problem.

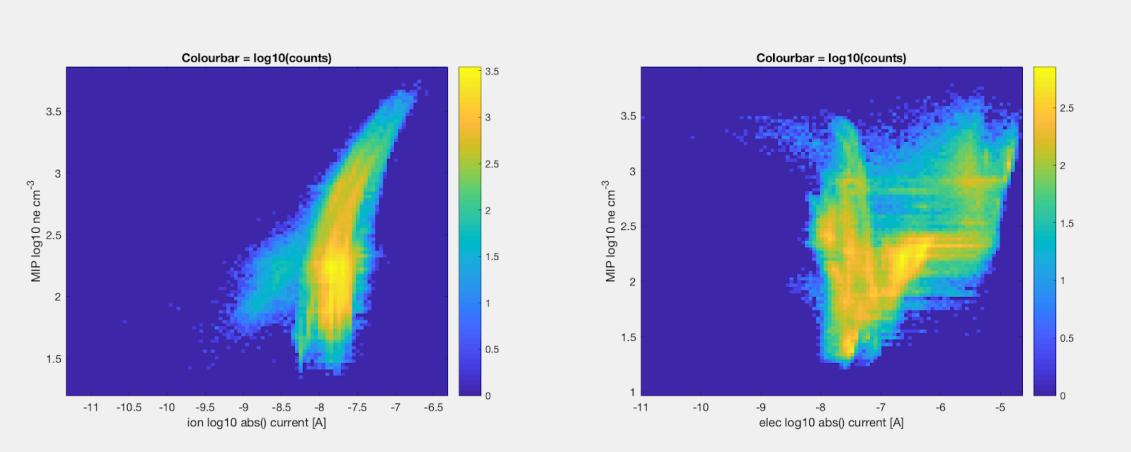

Figure 17: LAP currents vs coinciding MIP densities over the mission. **Left:** MIP density vs LAP1 current at negative bias voltage ($V_b < -15$ V, referred to as "ion current") , coloured by log10 counts in each bin. For large currents, there is a linear relation with electron density which continues also to lower densities if the probe is in shadow, but as it mostly is sunlit most data points at low densities fall in a cluster at typical photoemission current values (few tens of nA). **Right:** MIP density vs LAP1 electron currents (V_b >20 V), coloured by log10 counts in each bin. As density increases, so should the electron flux to the probe increase. However, the spacecraft potential becomes more negative with increased electron densities, and effectively shields LAP from the low energy part of the electron energy distribution, even at high positive bias potentials. Therefore, no clear linear trend in electron currents vs density can be seen. In fact, at regions of high densities, the currents seem to decrease with increasing density. As the cometary ions are generally positively charged, there are no energy constrains on the particles reaching the probe for a negative spacecraft so the ion current is immune to this effect.

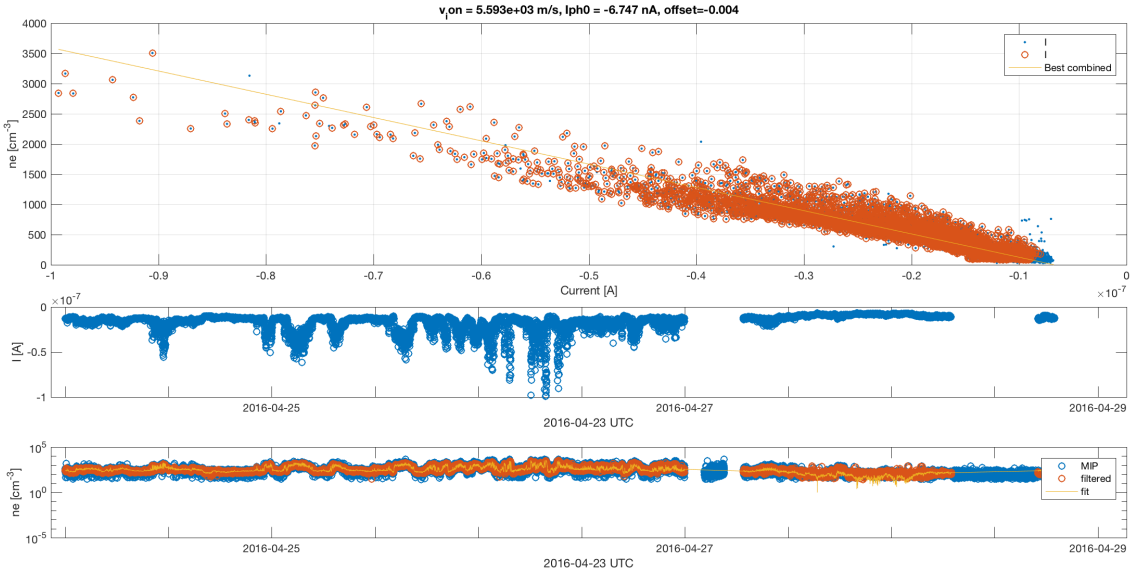

Figure 18: An example cross-calibration period of five days of LAP ion current measurements fitted against coinciding MIP measurements. **Top:** MIP density vs LAP ion current in red (and blue), orthogonal least-square fit in yellow resulting in a photoemission saturation current estimate of -6.7 nA and a effective ion flow speed of 5.6 km/s. **Middle:** All identified ion current measurements of a sunlit probe during a calibration window. **Bottom:** MIP densities (blue circles), MIP densities coinciding with LAP measurements (red circles) and cross-calibrated density estimate (yellow line). The current versions of this calibration used a 3-hour calibration window instead, but a clear linear relationship of the entire period is clearly visible even at large periods

The cross-calibrated data derived in the LAP archive differs from the cross-calibrated densities delivered by MIP mainly in that the cross-calibration fitting window is much wider (several hours or days compared to the MIP archive 20 minute window), allowing a wider coverage at the expense of lower absolute accuracy on shorter time scales. The coverage is further extended by calibration of LAP probe current or spacecraft potential to density by comparison to LAP plasma density from bias voltage sweeps in some environments where MIP data are not available. There are also differences in the evaluation of the quality of fits, and that the surviving fits is applied to the LAP data also outside of the fitting window. The general principle has been to generate the widest and best mission coverage of electron densities with sufficient number of sampled points to ensure a physical interpretation of each individual fit.

In the following two subsections we describe the LAP cross-calibration with MIP plasma density. Section 5.1 describes the cross-calibration of LAP ion currents. This is only used for the high time resolution plasma density data product known as N_EL. The low time resolution N_ED is always based on the LAP spacecraft potential estimate U_SC, which also N_EL can be when LAP is in E-field mode. The cross-calibration of U_SC with MIP is treated in Section 5.2.

5.1 Cross-calibrated electron density from LAP ion current (N_EL)

To observe the ion current, the bias voltage of a LAP probe is put to a negative value. For the bias values used, below -15 V, the current contribution from plasma electrons can usually be ignored. The ion current is described by $I = -I_{ph0} - I_{i0}(1 + qV_p/E_i)$, where I_{ph0} is the photoelectron saturation current, and $I_{i0} \propto n$. To this is added also the photoelectron emission current, which in this voltage range is independent of the bias voltage (unless the probe illumination changes). For a quasineutral plasma where density varies much faster than the EUV flux, ion energy and spacecraft potential, the combined ion and photoelectron current is therefore expected to vary linearly with MIP density, with coefficients in the linear relation changing on much longer timescales than the plasma density itself. This linear relationship is clearly visible in the example cross-calibration window in Figure 18, and also during the whole mission in Figure 17.

To convert ion currents to plasma density, we apply a cross-calibration window over three hours of ion current data (V_b<-15 V) which we fit to coinciding MIP density measurements in a least orthogonal squares sense. The window is stepped with one hour over the entire comet phase of the mission. If there are several LAP ion current measurements during the MIP density sampling interval, these ion current values

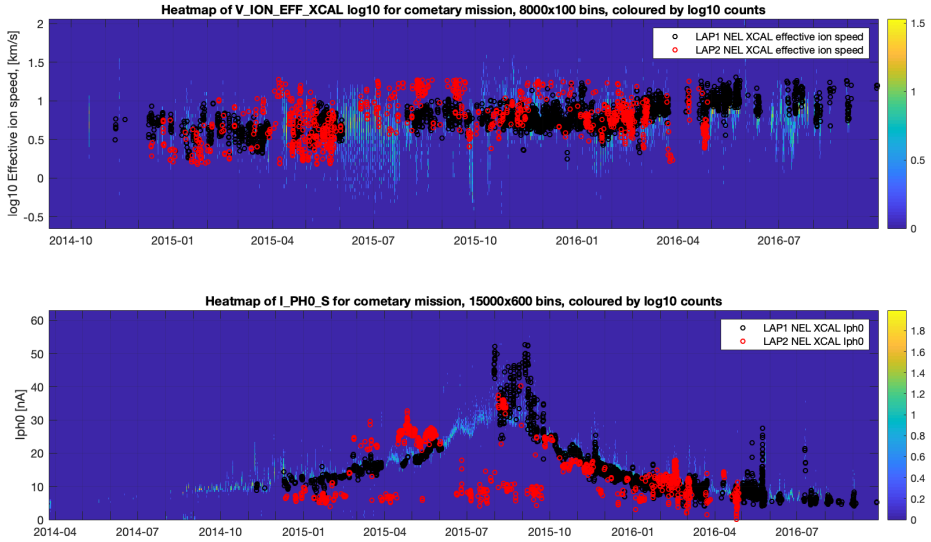

Figure 19: **Top:** 2D histogram of V_ION_EFF_XCAL (see Section 7) in 100 logarithmically spaced velocity bins, overplotted by the slope coefficient in ion cross-calbration converted to an effective ion velocity over the entire mission assuming an ion mass of 19 amu . LAP1 in black circles and LAP2 in red. **Bottom:** 2D histogram of I_PH0_S (Section 6) in 600 current bins, overplotted by the offset coefficient (photoemission) in ion cross-calbration plotted over the entire mission. LAP1 in black and LAP2 in red. LAP2 is marred by frequent illumination changes and also has less consistent photoemission according to other methods due to contamination, which is why it is not used for the photoemission data products discussed in Section 6.

are averaged. Measurements of ion currents on a shadowed probe are analysed separately. MIP points with a spectrum quality value or plasma signature quality below 0.3 are ignored. Poor or unphysical fits are identified and discarded using four criteria:

1. Poor correlation coefficient (< 0.7).
2. Unphysical slope estimate corresponding to negative ion energy.
3. Unphysical (positive) photoemission saturation current estimate
4. Clear ($>2\sigma$)outliers in slope or offset determination compared to full mission dataset.

During periods with low densities and few coinciding MIP and LAP data points (Before 2015-01-01, and during excursion around 2016-04-01) also mentioned in Section 4, the calibration instead fits a combined data set of scaled LAP sweep density estimates and MIP densities to currents. Also, it is applied over a larger calibration window (15 day window, 5 day step size) to improve the fitting procedure.

The cross-calibration coefficients obtained by this procedure can be physically interpreted as averages (not necessarily arithmetic means) of the photoemission current and the characteristic ion speed over the calibration window. Suitably scaled versions of both coefficients are plotted in Figure 19. The data in the upper plot is compared to the effective ion speed discussed in Section 7, though the coefficient from the ion current cross-calibration is a long term average based on current values while the effective ion speed is one value per sweep and based on the sweep slope. Of more interest is the photoelectron saturation current in the lower panel, which agrees very well with the higher time resolution photoemission current data products discussed in Section 6. The coefficients from the fits Figure 19 are archived with other calibration data products in the LAP archive (see EAICD).

The high time resolution cross-calibrated density available in the MIP data archive uses a shorter calibration window and is therefore considered to be better when available. We therefore only provide N_EL data when no cross-calibrated data are available in the MIP archive.

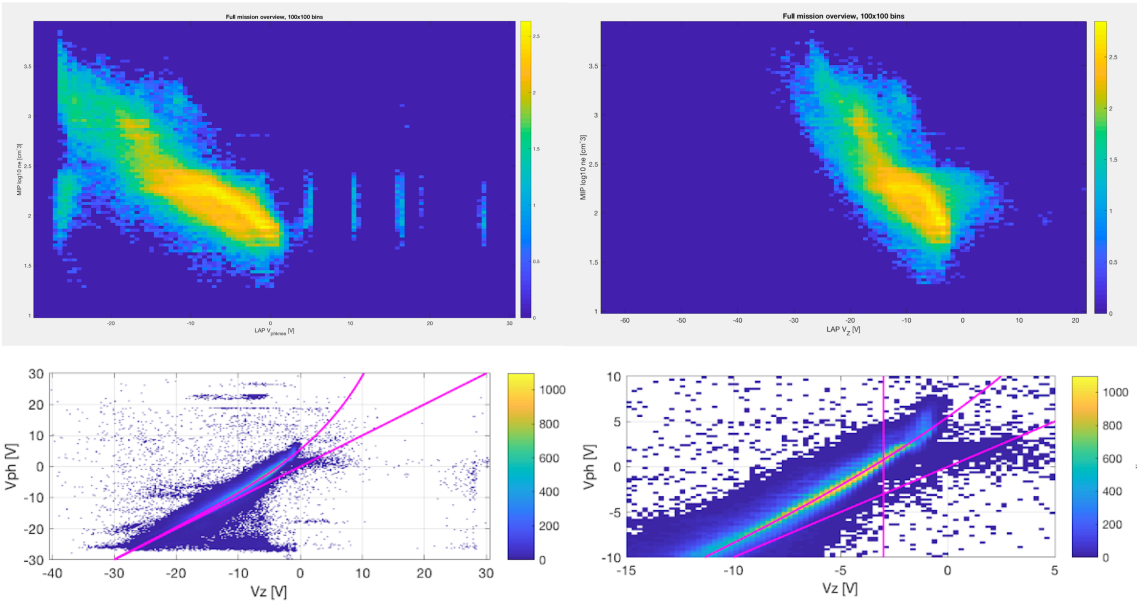

Figure 20: **Top left:** Simultaneous V_{ph} vs MIP density estimates over entire mission, 100x100 bins coloured by log10 counts. Several spurious detections of V_{ph} show up as thin lines at fixed potential. Also apparent is the upper sensitivity limit of the MIP LDL mode around 300 cm^{-3}. **Top right:** Simultaneous V_z vs MIP density estimates over entire mission, 100x100 bins coloured by log10 counts. V_z is less noisy than V_{ph}, but the upper sensitivity limit of MIP in LDL mode is also apparent. **Bottom left:** V_z vs V_{ph} over entire mission, coloured by counts. In purple, two asymptotes are plotted to map V_z (and conversely, U_1) to V_{ph}. As V_s goes towards 0 V or above, V_z is less sensitive to changes and does not go above 0 V except for misidentifications. **Bottom right:** Zoom in of V_z vs V_{ph} plot.

5.2 Cross-calibrated electron density from spacecraft potential (N_EL, N_ED)

When comparing V_{ph} with MIP and V_z with MIP as seen in Figure 20, we see that V_z and V_{ph} has a seemingly linear trend to the log of the density, but V_z does not reach positive potentials at the lowest densities. The plots in Figure 20 suggest that U_SC may be empirically connected to V_{ph} by defining a new variable

$$\text{U\_1} = \text{U\_SC} + 5.5\ \exp\left(\frac{\text{U\_SC}}{8.0}\right) \tag{1}$$

where the unit is volts. If V_z is above -3 V and there exists a coinciding V_{ph} that is above the corresponding U_1 value, we replace U_1 with that value. In this way we create a more seamless transition from pure V_z values at large negative U_SC values (as U_SC is based on V_z there, see Section 3 and the EAICD) to V_{ph} above -3 V, where it performs better than V_z. We do not archive U_1 as a spacecraft potential estimate as we cannot properly validate it. But as it does scale well with MIP data (Figure 21), we use U_1 as the parameter to cross-calibrate for the N_ED and N_EL density estimates.

For a negatively charged spacecraft, assuming the ion current and SEE current are mainly constant or negligible, the currents are balanced by an exponentially decaying electron current and a constant photoemission saturation current, I_{ph0}. We can then relate the electron density to spacecraft potential V_s by

$$n = A \exp\left(-\frac{eV_s}{k_B T_e}\right), \tag{2}$$

where A is some constant. If instead we have a proxy of the spacecraft potential U_1 such that U_1 = aV_s, where a is constant over the interval, then the equation becomes

$$n = P_2 \exp\left(P_1 \text{U\_1}\right), \tag{3}$$

where P_1 and P_2 are constants. Figure 21 indicates that the same trend seems reasonable also for positive potentials.

Similarly to the cross-calibration detailed in Section 5.1, we fit a line in an orthogonal least square sense to the natural logarithm of the MIP density, over a window of 3 days, iterating and stepping with

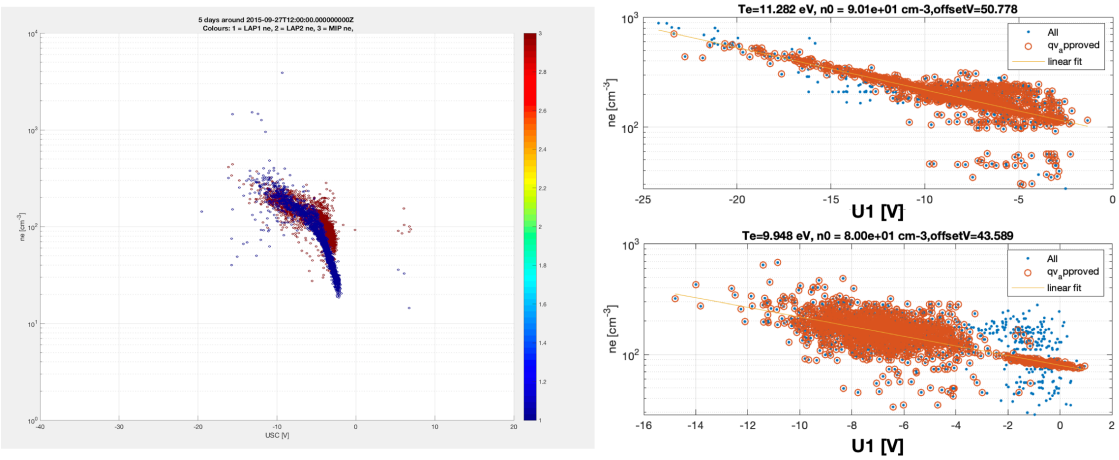

Figure 21: Comparison of MIP densities to spacecraft potential proxies (U_SC and U_1) over similar example periods. **Left:** MIP density (log) vs U_SC (in blue) and LAP sweep densities vs U_SC (red) over an example period from 2015-09-25 to 2015-09-30. A clear non-linear trend is visible. **Top right:** MIP density (log) vs U_1 for 2015-09-24 to 2015-09-26 **Bottom right:** MIP densities vs U_1 for 2015-09-27.

1 day over the entire mission. Again, as detailed in Section 5.1, when coinciding measurements are scarce, we instead fit a joint data set of MIP and scaled LAP sweep densities to U_1 over a larger timeframe (15 days) to improve the fit. MIP points with a spectrum quality value or plasma signature quality below 0.3 are ignored. Poor or unphysical fits are identified and discarded using three criteria:

1. Poor correlation coefficient (< 0.7).
2. Unphysical slope estimate corresponding to negative electron temperature.
3. Clear ($>2\sigma$) outliers in slope or offset determination compared to full mission data set.

The coefficients from the fits, converted to physical quantities in Figure 22 are archived with other LAP calibration products (see EAICD). Some examples of the NED density estimate is plotted in Figure 23 in comparison to MIP. NEL also contains cross-calibrated densities over the entire mission originating from high time resolution V_f data via U_1 to density. However, since there are cross-calibrated densities also in the MIP archive (considered to be of better quality as being based on shorter calibration windows) similarly derived for certain timeperiods, these intervals have been filtered out in the LAP delivered NEL dataset.

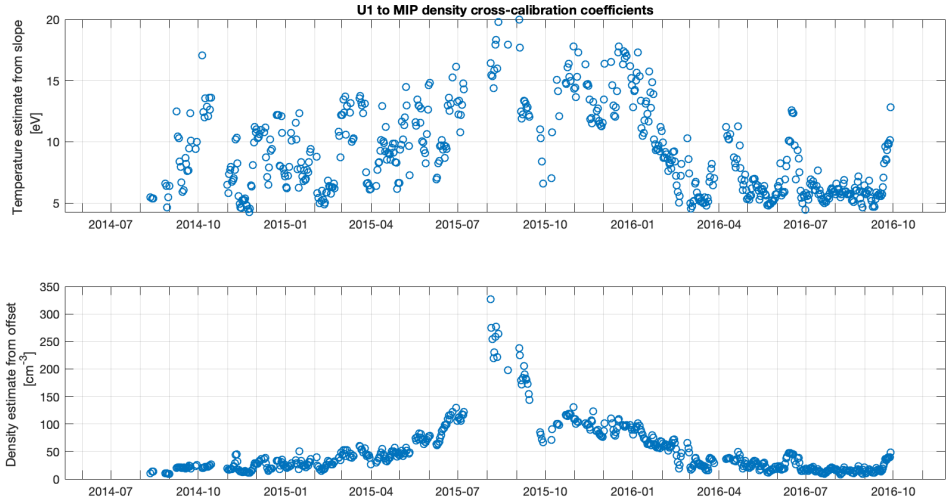

Figure 22: **Top:** Slope coefficient in U_1 cross-calibration converted to electron temperature for the entire mission. Note that the an offset from V_s to U_1 would lower the temperature estimate, and an offset has been applied in Figure 28. **Bottom:** Offset coefficient converted to units of density over the entire mission. Note that this is some hypothetical density where the currents to the spacecraft would balance at 0 V absolute potential. This estimate should co-vary with photoemission on the spacecraft

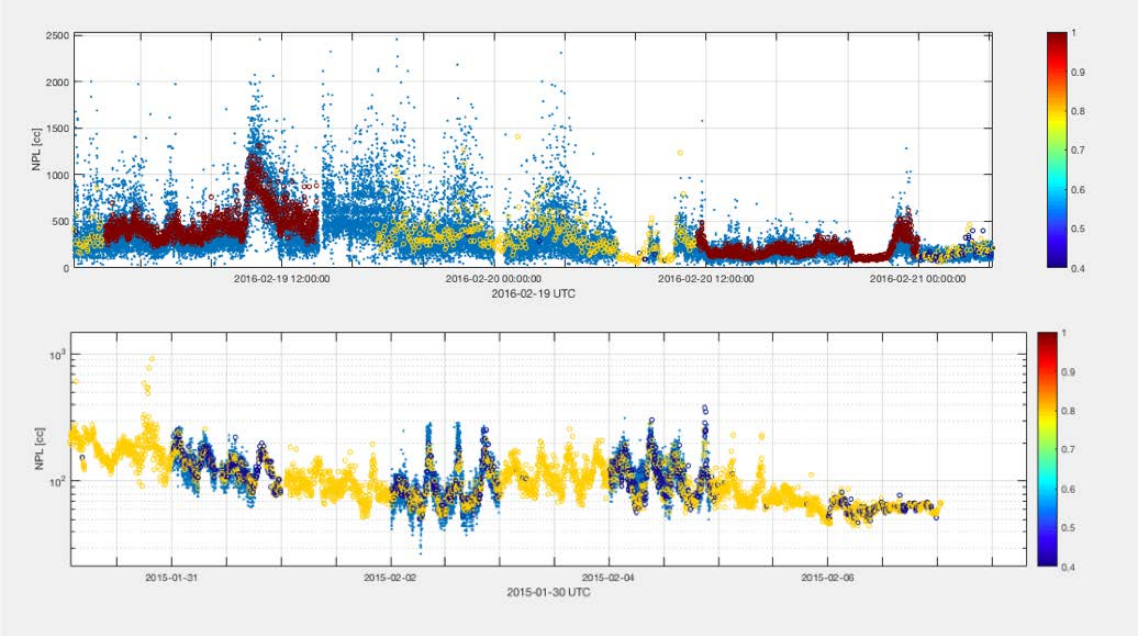

Figure 23: Two examples of NED density estimates (circles coloured by quality value) in comparison to MIP (blue dots)

6 Photoelectron emission current

When illuminated by solar EUV radiation, a conductor like a LAP probe will emit photoelectrons. When the electric field surrounding the probe is directed toward it on all sides, all photoelectrons escape resulting in the current being limited only by the photoelectron flux, which is set by the the UV intensity. This current, known as the photoelectron saturation current $I_{\rm ph0}$, thus acts as a solar EUV flux proxy. It adds to the currents due to collection of plasma ions and electrons by the probe. No other Rosetta instrument can measure $I_{\rm ph0}$, but as its value can be deduced from the LAP data in several different ways we can still do cross-calibration between these methods.

One method is based on fitting of individual LAP probe bias sweeps to theoretical expressions as illustrated in Figures 2 and 3. The LAP archive data includes $I_{\rm ph0}$ values derived in this way as the quantity I_PH0_S in the ASW files. The method allows the time resolution set by the sweep cadence (typically 160 s for LAP), but can show a lot of noise when the plasma density is high and variable.

We therefore devised a second method. In a plasma of density n a probe at negative voltage V will draw a current [Eriksson et al., 2017]

$$I = k\,n\left(1 + \frac{V}{E_{\rm i}}\right) + I_{\rm ph0}$$

from the surrounding plasma, where the first term represents the collected ions (assumed to have constant characteristic energy is $E_{\rm i}$) and the second the emission of photoelectrons, which should be a constant current $I_{\rm ph0}$ (k is a constant depending on $E_{\rm i}$). The derivative $\mathrm{d}I/\mathrm{d}V$ then is proportional to n. If we plot I versus $\mathrm{d}I/\mathrm{d}V$ for a set of sweeps obtained at different ion density n, we should be able to find $I_{\rm ph0}$ by fitting a line to these points and finding the intersection with the I axis, where $\mathrm{d}I/\mathrm{d}V = 0$ so that n and the first term in the equation above also are zero. That the method works and provides data with lower noise than the sweep fit method was shown by Johansson et al. [2017]. Photoemission current values obtained over one hour intervals in this way are available in the LAP archive as the quantity I_PHO_60M in the PHO files.

It is still possible that both could suffer from some form of residual instrumental offset. To close this loophole, we have investigated how the probe current changes when the illumination on the probe changes. This happens because of spacecraft pointing changes, in which a LAP probe may enter or exit the shade behind a spacecraft structure. As this method directly measures the change in current, it is immune to any offset in the instrument. Two examples is shown in Figure 24, indicating the high accuracy possible with this method. The obvious drawback with this method is that it does not allow any kind of regular sampling as it depends on the spacecraft pointing, which in turn depends on scientific planning as well as Rosetta's position in space around the comet. Nevertheless, it can still be used to verify the results obtained by the other methods.

A mission overview of the $I_{\rm ph0}$ values by these three methods is shown in Figure 25. The single-sweep fits show several outliers and lots of noise around perihelion (as expected, as the electron collection current here is much higher than the photoemission current due to the high plasma density), but the generally excellent agreement between all three methods validates the derivation of $I_{\rm ph0}$ and also provides the scientifically interesting result that the photoemission at perihelion was only about half as strong as expected [Johansson et al., 2017].

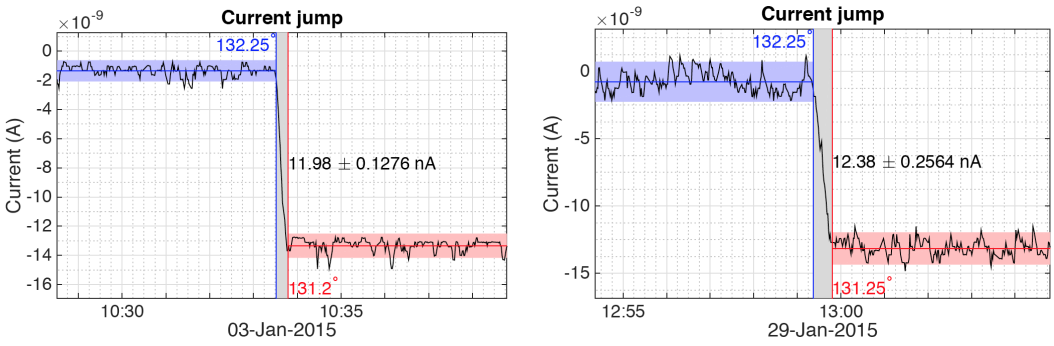

Figure 24: Two examples of the jump in the current flowing from LAP1 to the plasma as the probe moves from shadow to sunlight and hence starts to emit photoelectrons. The horizontal axes shows time (UT) in hours and minutes. The angle given is the solar aspect angle, explained in the LAP UG and EAICD documents and included in the LAP geometry files in the archive.

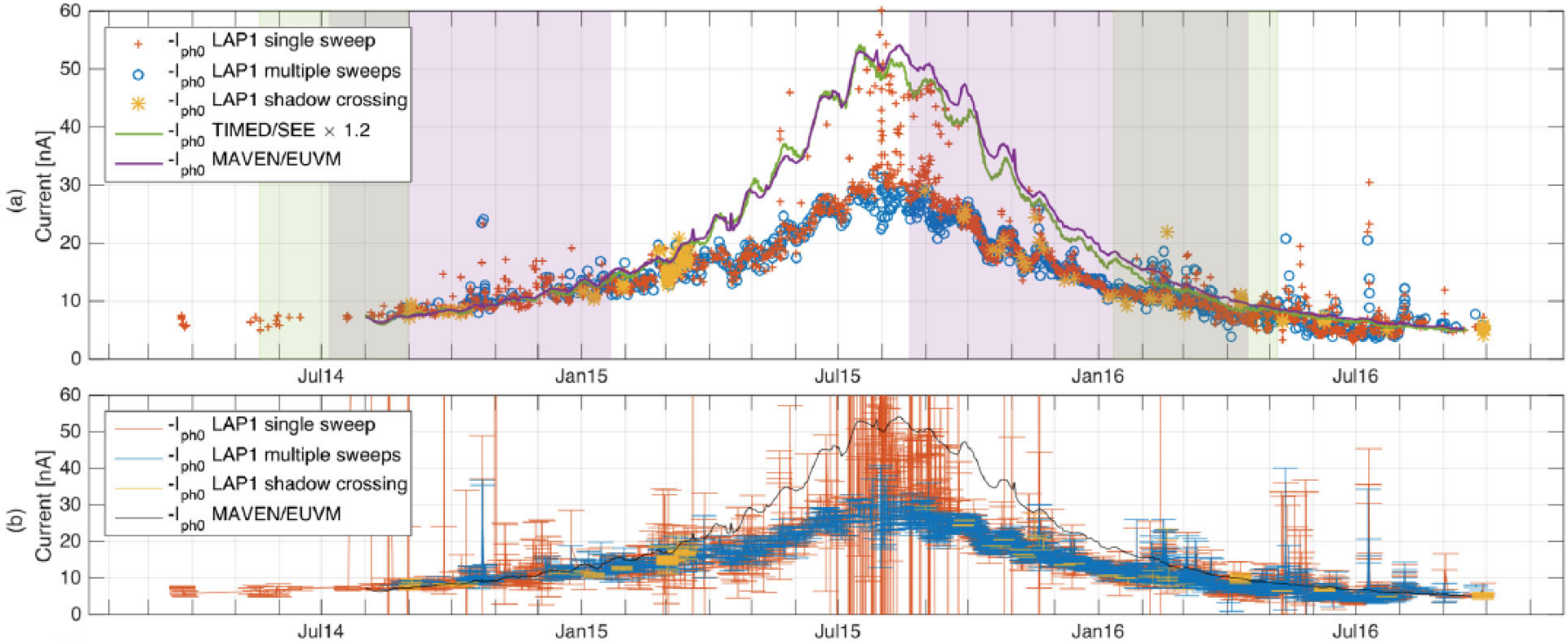

Figure 25: Panel(a) shows daily averages of I_{ph0} values derived by the three methods, as well as data propagated from Mars and Earth to Rosetta position. The higher noise and presence of outliers in the values derived from single sweeps (red) are highlighted in Panel (b), which also indicates the daily standard deviation. In yellow is the results of all shadow crossings, as explained in Figure 24. The three LAP methods all agree but differs from the propagated data for about a year around perihelion (August 2015) leading to the conclusion that something is quenching the photoemission on Rosetta, possibly UV absorption by nanodust grains at large distance. From Johansson et al. [2017].

Figure 19 contains comparisons to another LAP I_{ph0}, obtained in fitting ion currents to MIP densities. While this also derives from MIP and LAP data and is related to them, the general correspondence at least is further evidence for the consistency of the LAP measurements and our interpretation of them.

7 Ion effective speed

The LAP archive in the PSA includes a cross-calibrated LAP-MIP data product V_ION_EFF_XCAL. This is derived from the slope of the LAP current at as negative bias voltage as practical (see EAICD for details) combined with the density from a coincident (within one second) MIP density estimate, as shown in Figure 26. As illustrated in Figure 3, this region should be dominated by photoemission current (which should be constant) and ion current, with all the slope due to the ion current.

The speed derived in this way should be seen as an effective speed, whose interpretation relies on some assumptions. Disregarding possible (de-)focusing effects of ion pre-acceleration through the electrostatic field surrounding the spacecraft because of its (usually) negative charge, V_ION_EFF_XCAL will be the speed of the ions for the case of a monoenergetic distribution and one single ion mass (19 amu). For any other mass 19 ion speed distribution $f(v)$, V_ION_EFF_XCAL is the harmonic mean over the distribution,

$$\frac{\int f(v)\,\mathrm{d}v}{\int \frac{f(v)}{v}\,\mathrm{d}v}.$$

This means that for a broad distribution, lower speeds are have more influence on the resulting speed than higher speeds.

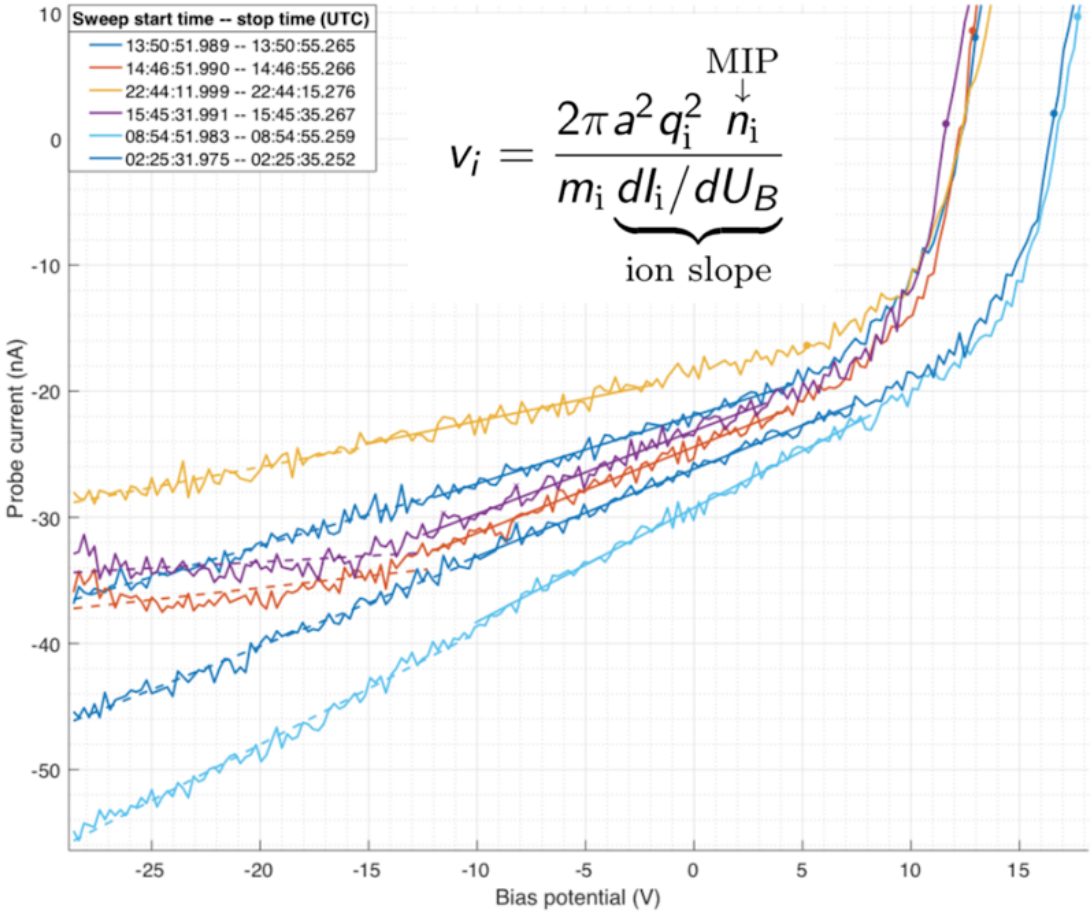

Figure 26: Examples of LAP ion effective speed derivation from LAP sweeps from November 20 and 21, 2015. Solid lines represent fitted ion slopes. The algorithm identifies and sorts out spurious low slopes at extreme negative bias potentials (presumably due to blocking of the ion flow by spacecraft surfaces). In the equation, v_i is the sought effective ion speed, a = 25 mm the radius of the spherical probe, q_i the ion charge (assumed to be one elementary charge), n_i the electron number density from MIP (assumed to equal the ion density), m_i the ion mass (assumed to be 19 amu) and $\mathrm{d}I_i/\mathrm{d}U_B$ slope of the probe current in the region where it is dominated by the ion current.

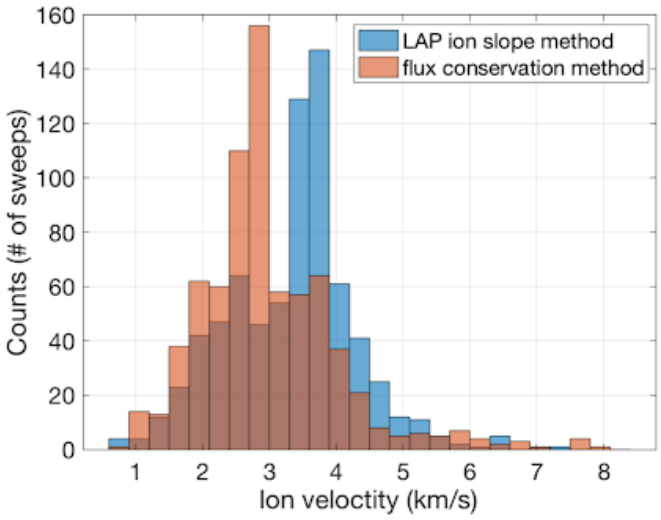

Figure 27: Histograms of V_ION_EFF_XCAL (blue) and the independent speed estimate by the flux conservation method (red), showing good statistical agreement. From Odelstad et al. [2018].

Due to the problems of measuring low energy ions with an instrument mounted on a negatively charged spacecraft, the velocity moments of ICA and IES are relatively insensitive to the lowest energy ions. The effective ion speed we derive therefore cannot be meaningfully compared to ICA or IES. However, Odelstad et al. [2018] used a validation method based on conservation of ion flux. Assuming constant ionization rate ν and no recombination in a spherically symmetric comet atmosphere where the neutral gas density n_n is inversely proportional to the squared cometocentric distance r and radial ion motion leads to a mean ion speed $n_\mathrm{n}\nu(r-R)/n_\mathrm{e}$, with R as the radius of the nucleus. The ionization rate ν can be calculated by independent methods [Heritier et al., 2018], and n_n and n_e are available from ROSINA-COPS and RPC-MIP, respectively, so this ion speed estimate is independent of LAP data. Exact similarity between this estimate and V_ION_EFF_XCAL is not expected, but investigations within the diamagnetic cavity (the only region where the assumptions behind the flux conservation method are likely to be satisfied) provided similar statistics for the two methods (Figure 27).

Figure 19 contains another comparison of V_ION_EFF_XCAL, this time to another measure of the effective ion speed: the fit coefficient obtained when fitting ion currents to MIP densities. While this also derives from MIP and LAP data, it is independent from V_ION_EFF_XCAL in that it does not use the LAP sweeps and the slope of the current-voltage characteristic but the value of the current at fixed bias. The general correspondence at least is further evidence for the consistency of the LAP measurements and our interpretation of them.

8 Electron temperature

8.1 LAP sweep electron temperature T_E

The standard technique for obtaining the electron temperature T_e is to fit an exponential function to the part of the probe current-voltage characteristic, as measured by a voltage bias sweep (see Figures 2 and 3). In practice, a linear function is fitted to the logarithm of the current, which is how the LAP electron temperature estimate T_E is derived. Before such a fit can be done, the relevant region has to be identified in the sweep by finding the s/c potential (as described in (Sections 2 and 3), and the current contributions due to photoelectron emission and ion collection removed (by linear fit to the most negative part of the sweep, see EAICD). Together with natural and artificial noise in the current, this procedure inevitably introduces random errors to the process, particularly as the electron distribution may not be well described by a Maxwellian. Several studies show several coexisting electron populations at 67P [e.g. Clark et al., 2015, Broiles et al., 2016b, Madanian et al., 2016, Eriksson et al., 2017, Gilet et al., 2017, Madanian et al., 2017, Engelhardt et al., 2018], some of them better described by a kappa distribution [Broiles et al., 2016a]. As a result, the T_E data product is quite noisy, which can be seen in Figure 28. While some of this noise is physical, random errors are significant. As described in Section 4, we therefore do not use the value T_E from each sweep as electron temperature when deriving a plasma density from the slope of the LAP sweeps but assumed values giving good statistical agreement with MIP derived densities.

8.2 LAP-MIP electron temperature T_E_XCAL

A prominent feature in the LAP sweep data set are the intermittent presence of very steep slope at positive bias voltages, much higher than the slope found in the exponential region from which we determine T_E (c.f. Section 8.1 above). As discussed by Eriksson et al. [2017] and Engelhardt et al. [2018], this is consistent with the presence of a second electron population of cold electrons, with characteristic energy on the order of 0.1 eV or below. The presence of this population has also been verified independently by MIP [Gilet et al., 2017]. The exponential region will be dominated by the warm electrons, meaning the T_E value pertains to that population, while the sweep slope at positive bias potentials will be dominated by the cold electrons which are easier to attract. We should thus be able to obtain an estimate of also the cold electron temperature.

As one cannot recover the electron temperature from the slope of the attracting electron current without knowing the density, and knowing that due to the depletion of electrons close to the probe, the LAP N_E_FIX_T_E estimate is often lower than expected as discussed in Section 4, we instead use the simultaneous density detection from MIP to estimate the electron temperature from the slope, if available. Generally, we expect this temperature to match the T_E estimate when the spacecraft potential does not significantly repel the electron density i.e. when the spacecraft potential is close to or above 0 V, or when the population of electrons with energies below the spacecraft potential is insignificant. This can also be seen in Figure 28, for which we intermittently find very cold T_E_XCAL estimates around 0.1 eV, and intermittently find values on the order of 5-10 eV, which is the mission wide average for the T_E estimate. If LAP does not reach sufficiently potentials to access the cold electrons simply because it was outside the sweep range, but MIP can, we expect this estimate to be much higher than the actual temperature, as well as our other estimates. Therefore all values above 30 eV have been removed, but several outliers above T_E remains. The availability of LAP1 sweeps with simultaneous MIP density estimates limits the availability of T_E_XCAL. Gilet et al. [2017] found, when the electron distribution is within certain range of parameters, that MIP can obtain an estimate of the temperature ratio between a cold and a warm electron population via the acoustic electron resonance, and we find these cold electron temperatures to be quite comparable to T_E and T_E_XCAL when steep slopes are apparent.

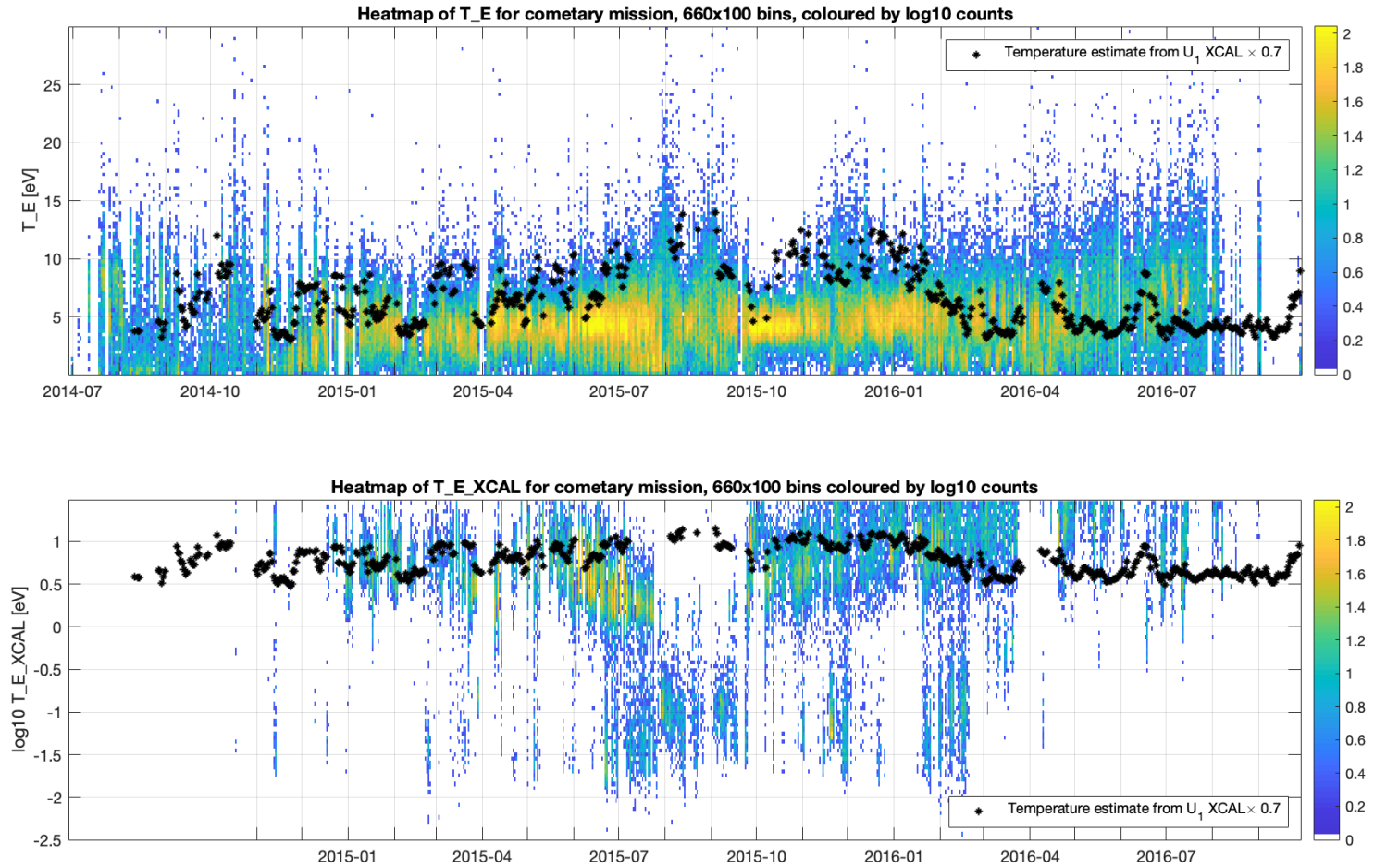

Figure 28: Density plots of electron temperatures from LAP bias sweeps coloured by log10 counts, overplotted with a scaled U_1 cross-calibration estimate from Section 5.2in black stars. As discussed in Sections 5.2 & 3 the scaling comes from U_1 being a proxy some factor away from the spacecraft potential V_S. **Top:** T_E vs time in 100 linearly spaced temperature bins. **Bottom:** T_E_XCAL (log10) vs time in 100 logarithmically spaced temperature bins. T_E_XCAL is not meant to be understood as an estimate for the total electron temperature for the entire mission, but does indicate the presence of cold electrons in LAP sweeps. The availability of LAP1 sweeps with simultaneous MIP density estimates limits the availability of T_E_XCAL.

References

T. W. Broiles, J. L. Burch, K. Chae, G. Clark, T. E. Cravens, A. Eriksson, S. A. Fuselier, R. A. Frahm, S. Gasc, R. Goldstein, P. Henri, C. Koenders, G. Livadiotis, K. E. Mandt, P. Mokashi, Z. Nemeth, E. Odelstad, M. Rubin, and M. Samara. Statistical analysis of suprathermal electron drivers at 67P/Churyumov-Gerasimenko. *Monthly Notices of the Royal Astronomical Society*, 462:S312–S322, November 2016a. doi: 10.1093/mnras/stw2942. URL https://dx.doi.org/10.1093/mnras/stw2942.

T. W. Broiles, G. Livadiotis, J. L. Burch, K. Chae, G. Clark, T. E. Cravens, R. Davidson, A. Eriksson, R. A. Frahm, S. A. Fuselier, J. Goldstein, R. Goldstein, P. Henri, H. Madanian, K. Mandt, P. Mokashi, C. Pollock, A. Rahmati, M. Samara, and S. J. Schwartz. Characterizing cometary electrons with kappa distributions. *Journal of Geophysical Research (Space Physics)*, 121:7407–7422, August 2016b. doi: 10.1002/2016JA022972. URL https://dx.doi.org/10.1002/2016JA022972.

G. Clark, Broiles, T. W., Burch, J. L., Collinson, G. A., Cravens, T., Frahm, R. A., Goldstein, J., Goldstein, R., Mandt, K., Mokashi, P., Samara, M., and Pollock, C. J. Suprathermal electron environment of comet 67P/Churyumov-Gerasimenko: Observations from the Rosetta ion and electron sensor. *Astronomy & Astrophysics*, 2015. doi: 10.1051/0004-6361/201526351. URL http://dx.doi.org/10.1051/0004-6361/201526351.

I. A. D. Engelhardt, A. I. Eriksson, E. Vigren, X. Valiières, M. Rubin, N. Gilet, and P. Henri. Cold electrons at comet 67P/Churyumov-Gerasimenko. *Astronomy and Astrophysics*, 616:A51, Aug 2018. doi: 10.1051/0004-6361/201833251. URL https://doi.org/10.1051/0004-6361/201833251.

A. I. Eriksson, I. A. D. Engelhardt, M. André, R. Boström, N. J. T. Edberg, F. L. Johansson, E. Odelstad, E. Vigren, J.-E. Wahlund, P. Henri, J.-P. Lebreton, W. J. Miloch, J. J. P. Paulsson, C. Simon Wedlund, L. Yang, T. Karlsson, R. Jarvinen, T. Broiles, K. Mandt, C. M. Carr, M. Galand, H. Nilsson, and C. Norberg. Cold and warm electrons at comet 67P/Churyumov-Gerasimenko. *A&A*, 605:A15, 2017. doi: 10.1051/0004-6361/201630159. URL https://doi.org/10.1051/0004-6361/201630159.

N. Gilet, P. Henri, G. Wattieaux, M. Cilibrasi, and C. Béghin. Electrostatic potential radiated by a pulsating charge in a two-electron temperature plasma. *Radio Science*, 52(11):1432–1448, 2017. ISSN 1944-799X. doi: 10.1002/2017RS006294. URL http://dx.doi.org/10.1002/2017RS006294.

K.L. Heritier, M. Galand, P. Henri, F.L. Johansson, A. Beth, A.I. Eriksson, X. Vallières, K. Altwegg, J.L. Burch, C. Carr, E. Ducrot, R. Hajra, and M. Rubin. Plasma source and loss at comet 67P during the Rosetta mission. *Astronomy & Astrophysics*, 618, 2018. doi: 10.1051/0004-6361/201832881. URL https://dx.doi.org/10.1051/0004-6361/201832881.

F. L. Johansson, E. Odelstad, J. J. P. Paulsson, S. S. Harang, A. I. Eriksson, T. Mannel, E. Vigren, N. J. T. Edberg, W. J. Miloch, C. Simon Wedlund, E. Thiemann, F. Eparvier, and L. Andersson. Rosetta photoelectron emission and solar ultraviolet flux at comet 67P. *Monthly Notices of the Royal Astronomical Society*, 469:S626–S635, July 2017. doi: 10.1093/mnras/stx2369. URL https://dx.doi.org/10.1093/mnras/stx2369.

H. Madanian, T. E. Cravens, A. Rahmati, R. Goldstein, J. Burch, A. I. Eriksson, N. J. T. Edberg, P. Henri, K. Mandt, G. Clark, M. Rubin, T. Broiles, and N. L. Reedy. Suprathermal electrons near the nucleus of comet 67P/Churyumov-Gerasimenko at 3 au: Model comparisons with Rosetta data. *Journal of Geophysical Research: Space Physics*, 121, 2016. ISSN 2169-9402. doi: 10.1002/2016JA022610. URL http://dx.doi.org/10.1002/2016JA022610. 2016JA022610.

H. Madanian, T. E. Cravens, J. Burch, R. Goldstein, M. Rubin, Z. Nemeth, C. Goetz, C. Koenders, and K. Altwegg. Plasma environment around comet 67P/Churyumov-Gerasimenko at perihelion: Model comparison with Rosetta data. *The Astronomical Journal*, 153(1):30, 2017. doi: 10.3847/1538-3881/153/1/30. URL http://dx.doi.org/10.3847/1538-3881/153/1/30.

E. Odelstad. *Plasma environment of an intermediately active comet : Evolution and dynamics observed by ESA's Rosetta spacecraft at 67P/Churyumov-Gerasimenko*. PhD thesis, Uppsala University, Space Plasma Physics, 2018. URL http://urn.kb.se/resolve?urn=urn:nbn:se:uu:diva-356426.

E. Odelstad, A. I. Eriksson, N. J. T. Edberg, F. Johansson, E. Vigren, André M., C.-Y. Tzou, C. Carr, and E. Cupido. Evolution of the plasma environment of comet 67P from spacecraft potential measurements by the Rosetta Langmuir probe instrument. *Geophys. Res. Lett.*, 42(23):10,126–10,134, 2015. ISSN 1944-8007. doi: 10.1002/2015GL066599. URL http://dx.doi.org/10.1002/2015GL066599.

E. Odelstad, G. Stenberg-Wieser, M. Wieser, A. I. Eriksson, H. Nilsson, and F. L. Johansson. Measurements of the electrostatic potential of Rosetta at comet 67P. *Monthly Notices of the Royal Astronomical Society*, 469:S568–S581, July 2017. doi: 10.1093/mnras/stx2232. URL https://dx.doi.org/10.1093/mnras/stx2232.

E. Odelstad, A. I. Eriksson, F. L. Johansson, E. Vigren, P. Henri, N. Gilet, K. L. Heritier, X. Vallières, M. Rubin, and André M. Ion velocity and electron temperature inside and around the diamagnetic cavity of comet 67P. *Journal of Geophysical Research: Space Physics*, 123(7):5870–5893, 2018. doi: 10.1029/2018JA025542. URL https://agupubs.onlinelibrary.wiley.com/doi/abs/10.1029/2018JA025542.